Structural, Elastic, Electronic and Optical Properties Study of Hexahalometallate Single Crystals X_2SnBr_6 (X = Rb, Cs)

L. Krache[a], M.A. Ghebouli[b,c], B. Ghebouli[d],
M. Fatmi[c,*], T. Chihi[c] AND S.I. Ahmed[e, ORCID]

[a]PQSD Laboratory, Department of Physics, Faculty of Science, University Ferhat Abbas of Setif 1, Setif, 19000, Algeria
[b]Department of Chemistry, Faculty of Technology, University of Mohamed Boudiaf, M'sila, 28000, Algeria
[c]Research Unit on Emerging Materials (RUEM), University Ferhat Abbas of Setif 1, Setif, 19000, Algeria
[d]Laboratory of Studies Surfaces and Interfaces of Solids Materials, Department of Physics, Faculty of Science, University Ferhat Abbas of Setif 1, Setif 19000, Algeria
[e]Department of Physics, College of Science, Taif University, P.O. Box 11099, Taif 21944, Saudi Arabia

We carried out a theoretical study on hexahalometallate single crystals X_2SnBr_6 (X = Rb, Cs) with the density functional theory framework, using generalized gradient approximation of the Perdew, Burke, and Ernzerhof and Heyd–Scuseria–Ernzerhof hybrid functional. The lattice constant of the compounds Cs_2SnBr_6 and Rb_2SnBr_6 is consistent with the experimental data currently available, with an uncertainty of 0.04% and 0.07%, respectively. For the first time, the elastic moduli of Cs_2SnBr_6 at equilibrium and under pressure effect were estimated. When fitted to the Birch–Murnaghan equation of state, the bulk modulus of Cs_2SnBr_6 and Rb_2SnBr_6 obtained using the generalized gradient approximation optimization is closer to the experimental one. The interatomic distances of Cs_2SnBr_6 are greater than those of Rb_2SnBr_6, because these distances are proportional to the radius of Cs (1.73 Å) and Rb (1.64 Å). The direct band gap Γ–Γ of 1.272 eV and 1.1019 eV for, respectively, Cs_2SnBr_6 and Rb_2SnBr_6 explains their semiconducting character. The Sn-s state dominates in the conduction band minima, indicating that Sn and Br are in ionic connection in both Cs_2SnBr_6 and Rb_2SnBr_6.

topics: hexahalometallate, band structure, band gap, absorption

1. Introduction

Inorganic halide perovskites attract researchers because of their application as light-absorbing materials in photovoltaic cells. This family of hexahalometallate materials usually crystallizes in the face-centered cubic of the antifluorite structure K_2PtCl_6 with the space group $Fm3m$. The formula X_2MA_6 describes these materials, where X is an alkaline metal, A is a halogen, and M is a polyvalent or heavy transition metal. In the antifluorite structure, the M cation occupies one face of a centered cube and is surrounded by an octahedron by the A anion located at $\left(\frac{1}{4}, \frac{1}{4}, \frac{1}{4}\right)a_0$ along the equivalent of six cubic axes. The X ion is arranged in eight-fold cubic coordination around the M cation located at $\left(\frac{1}{4}, \frac{1}{4}, \frac{1}{4}\right)a_0$, and each X ion is shared into four M cations. The M cation is coordinated by 12 A anion, while the X ion presents a coordination number

of 24 by an A anion. The potential for these materials to be used as absorbent materials for solar cells is what sparks interest in study of hexahalometallate X_2SnBr_6 (X = Rb, Cs) materials. This work uses the generalized gradient of the Perdew, Burke, and Ernzerhof (GGA-PBESOL) approximation and the Heyd–Scuseria–Ernzerhof (HSE) hybrid functional to derive sufficient physical parameters for X_2SnBr_6 (X = Rb, Cs). For a study carried out by other researchers, the geometry of the double perovskite structure depends on the chemical composition, temperature, and pressure [1]. The transition point in hexahalometallate X_2MA_6 semiconductors is shifted to lower temperatures (< 77 K) with increasing size of the central metal atom (M) and decreasing size of the halogen ligands (A) [2]. Due to their high absorption coefficient, low reflectivity, low cost, variable band gap and high conversion efficiency for solar applications [3–5], the

complex halides X_2SnBr_6 (X = Rb, Cs) are of interest to researchers as absorbent materials [6, 7]. Lead-free perovskites, based on inorganic halides X_2SnBr_6 (X = Rb, Cs), are stable and absorb light in solar cells [8]. N. Wruk et al. [9] experimentally studied the elastic constants of Rb_2SnBr_6 at ambient temperature and equilibrium pressure by measuring ultrasonic wave velocity and Brillouin scattering. The investigation carried out by Yong Tang et al. [10] evaluates that lead-free perovskite Rb_2SnBr_6 has a small effective mass, a direct band gap, and a high optical absorption coefficient of 10^5 cm^{-1}; hence, it may be a potential candidate for an excellent light absorbing material [10]. M. Razzaq and M. Tarikul [11] determined the elastic constants of Rb_2SnBr_6 at 0 GPa and a direct band gap of 1.228 eV. The possibility to find suitable optoelectronic quantities such as band gap, absorption, reflectivity, refractive index, and dielectric constant motivated us to investigate hexahalometallate X_2SnBr_6 (X = Rb, Cs) in a cubic structure using first-principles calculations.

2. Method

We performed geometry optimization using the plane wave pseudopotential method as implemented in the CASTEP code [12]. The interaction between valence electrons and ion cores is represented by the ultra-soft type of Vanderbilt pseudopotential [13]. The exchange–correlation effect is described by GGA-PBESOL [14] and the HSE hybrid functional. The use of Monkhorst–Pack points on the grid $8 \times 8 \times 8$ and the cut-off energy of 660 eV are necessary for both the best convergence of structures and energies [15]. Optical quantities must be calculated using a dense mesh made of evenly spaced $20 \times 20 \times 20$ k-points. The Broyden–Fletcher–Goldfarb–Shanno minimization method [16] determines the structural parameters and offers a quick method to locate the lowest energy structure. The tolerance for geometry optimization was set as the difference of the total energy 5×10^{-6} eV/atom, the maximum ionic Hellmann–Feynman force 10^{-2} eV/Å and the maximum stress 2×10^{-2} eV/Å^3.

3. Results and discussions

3.1. Study of internal structure

In Fig. 1, we display the crystal structure of Rb_2SnBr_6. We place the Sn atom in the middle of the Br octahedron, which is made up of four Br atoms. The Rb atom resides in interstitial sites. At ambient temperatures, X_2SnBr_6 (X = Rb, Cs) adopts a cubic structure with the space group $Fm3m$. The locations of the X, Sn, and Br atoms are $(0, 0, 0) a_0$, $(0, x, 0) a_0$, and $(0, x, x) a_0$, respectively. Table I contains X_2SnBr_6 (X = Rb, Cs) lattice constant, bulk modulus and its pressure
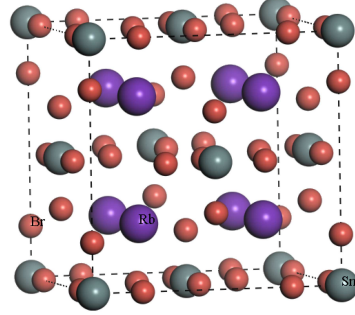

Fig. 1. Crystal structure of the double perovskite Rb_2SnBr_6.

TABLE I

The lattice constant (a), internal coordinate (x), bulk modulus (B_0) and its pressure derivative (B') and elastic constants (C_{ij}) for Cs_2SnBr_6 and Rb_2SnBr_6. Notation: B_0^{**} — bulk modulus calculated from elastic constant, B_0^* — bulk modulus obtained from fit Birch.

	This work	Experimental	Other calculations
Cs_2SnBr_6			
a [Å]	10.8415	10.837 [17]	10.863 [18]
			10.73 [19]
x	0.24215	0.245	0.24295 [19]
B_0^* [GPa]	11.16	11 [18]	
B' [GPa]	7.168		
C_{11} [GPa]	11.49		
C_{12} [GPa]	6.90		
C_{44} [GPa]	6.17		
B_0^{**} [GPa]	8.43		
Rb_2SnBr_6			
a [Å]	10.6322	10.64 [9]	10.75 [11]
x	0.24627	0.245	
B_0^* [GPa]	13.96		
B' [GPa]	06.481		
C_{11} [GPa]	15.04	19.00 [9]	28.7 [11]
C_{12} [GPa]	11.26	10.40 [9]	10.99 [11]
C_{44} [GPa]	8.63	8.40 [9]	13.2 [11]
B_0^{**} [GPa]	12.52	13.30 [9]	16.89 [11]

derivative. The lattice constant is closer to the experimental value and agree well with the theoretical one reported in the literature [8, 9, 11, 17–19], where the uncertainty is 0.04% and 0.07% (0.18% and 1.1%) for the case X = Rb and X = Cr, respectively. The bulk modulus of Cs_2SnBr_6 calculated using the fit scheme $P(V/V_0)$ agrees well with the available experimental data [18], where the uncertainty is 1.4%. We list the bond lengths of Rb_2SnBr_6 and Cs_2SnBr_6 at equilibrium in Table II.

TABLE II

Interatomic distances in Rb_2SnBr_6 and Cs_2SnBr_6.

	Br–Sn [Å]	Br–Br [Å]	Br–Rb [Å]	Rb–Sn [Å]	Rb–Rb [Å]	Br–Cs [Å]	Sn–Cs [Å]	Cs–Cs [Å]
Rb_2SnBr_6	2.61845	3.70304	3.75926	4.60388	5.31611			
Cs_2SnBr_6	2.62527	3.71269				3.83400	4.69451	5.42075
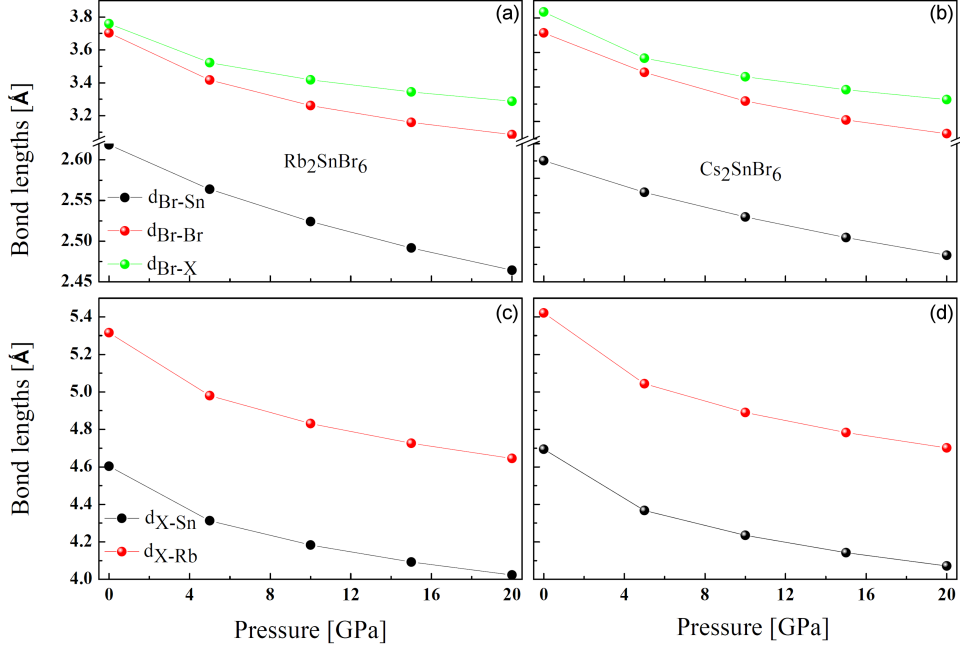
Fig. 2. Effect of pressure on bond lengths in double perovskites (a, c) Rb_2SnBr_6 and (b, d) Cs_2SnBr_6.

The fact that the distances are related to the X radius explains why the bond lengths of Cs_2SnBr_6 are longer than those of Rb_2SnBr_6. Additionally, the X–Br distances are wider than the Sn–X link ones.

The effect of pressure on bond lengths is visualized in Fig. 2. All bond lengths decrease monotonously with increasing pressure and become short during compression. Figure 3 represents the effect of pressure on the internal coordinate of the Br atom in Rb_2SnBr_6 and Cs_2SnBr_6. The internal coordinate of the Br atom in Cs_2SnBr_6 is lower than that of the Br atom in Rb_2SnBr_6 and this can be explained by the fact that it is inversely proportional to Cs (1.73 Å) and Rb (1.64 Å) radius. We find that the internal coordinate x of the Br atom increases with increasing pressure. Figure 4 visualized the dependence of normalized volume to pressure for Rb_2SnBr_6 and Cs_2SnBr_6 as fitted to the Birch–Murnaghan equation of state. We report the bulk modulus and its pressure derivative with the previous results in Table I. The bulk modulus calculated from GGA-PBESOL is closer to the experimental value [18]. The bulk modulus (pressure derivative) of Cs_2SnBr_6 and Rb_2SnBr_6 are 11.16 GPa and 13.96 GPa (7.168 and 5.481), respectively. We note that the Birch fit of Cs_2SnBr_6 is consistent with
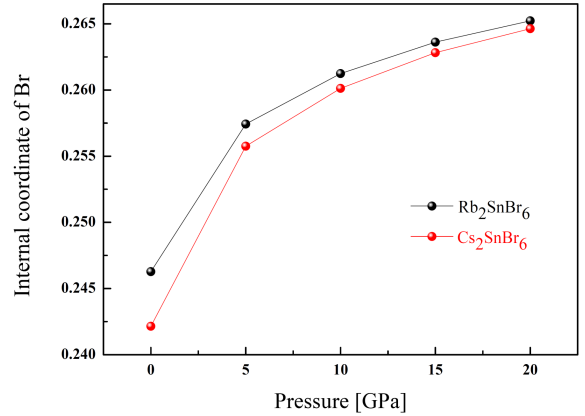
Fig. 3. Internal coordinate of the Br atom in Rb_2SnBr_6 and Cs_2SnBr_6 versus pressure.

the experimental result [18]. The ultra-low value of the bulk modulus demonstrates the soft nature of Cs_2SnBr_6 and Rb_2SnBr_6. The bulk modulus of Rb_2SnBr_6 and Cs_2SnBr_6 is weaker; normalized volume values smaller than 0.65 induce pressure higher than 20 GPa and other phases can be obtained. There is no experimental data for the left side of the minimum near equilibrium, therefore we only

TABLE III

The bulk modulus B [GPa], shear modulus G [GPa], Young's modulus E_H [GPa], Poisson's ratio, anisotropy factor A^U and B_H/G_H ratio for Rb_2SnBr_6 and Cs_2SnBr_6.

Material	B [GPa]			G [GPa]			E_H [GPa]	σ_H	A^U	B_H/G_H
	B_V	B_R	B_H	G_V	G_R	G_H				
Rb_2SnBr_6	12.255	12.255	12.25	5.9345	3.5584	4.7465	12.642	0.33177	3.33865	2.58
Cs_2SnBr_6	8.4368	8.4368	8.4368	4.6229	3.6796	4.1512	10.699	0.28865	1.28185	2.03

TABLE IV

The predicted maximum and minimum values of Young's modulus E [GPa], linear compressibility β [GPa], shear modulus [GPa], and Poisson's ratio σ for Cs_2SnBr_6 and Rb_2SnBr_6.

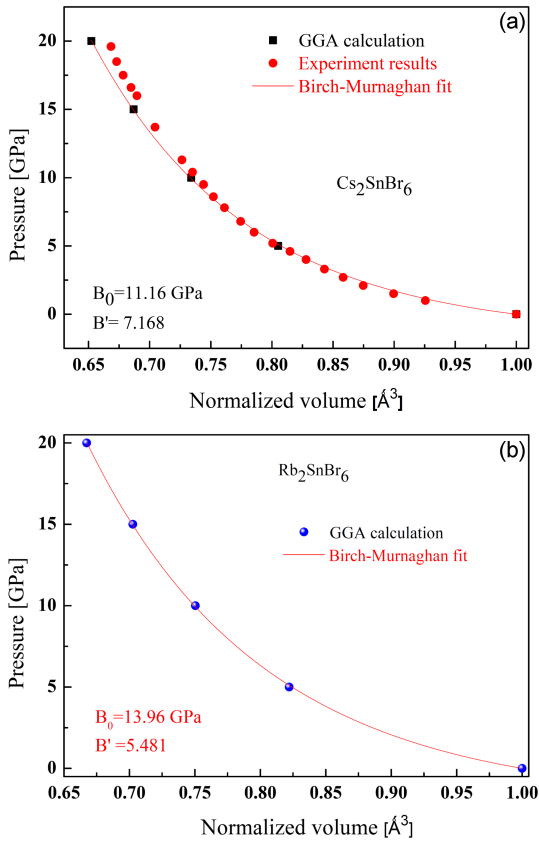| Material	Young's modulus		Linear compressibility		Shear modulus		Poisson's ratio	
	E_{min}	E_{max}	β_{min}	β_{max}	G_{min}	G_{max}	σ_{min}	σ_{max}
Rb_2SnBr_6	5.4019	21.054	26.614	26.614	1.8913	8.63	0.2926	0.9676
Cs_2SnBr_6	6.3007	14.898	39.509	39.509	2.2903	6.178	0.10097	0.66208

Fig. 4. Pressure dependence on the normalized volume for (a) Cs_2SnBr_6 and (b) Rb_2SnBr_6.

used data for the right side. The pressure 20 GPa and the normalized volume 0.65 are closer to the experimental values located around 19 GPa and 0.66, respectively. This proves that the obtained values are reasonable.

3.2. Elastic constants and mechanical parameters

The elastic constants are calculated using the theoretical equilibrium volume. We summarize the computed elastic moduli of Cs_2SnBr_6 and Rb_2SnBr_6 at equilibrium in Table I. There are no experimental and theoretical data for the elastic constants of Cs_2SnBr_6, consequently, future experimental measurements will test our prediction computation. The elastic moduli of Rb_2SnBr_6 are in reasonable agreement with the experimental values [9] and the theoretical data [11]. The elastic constants of Cs_2SnBr_6 and Rb_2SnBr_6 are smaller due to their larger reticular distances and therefore lower Coulomb binding forces. The elastic moduli of Cs_2SnBr_6 and Rb_2SnBr_6 satisfied the relationships mentioned below

$$0 < C_{11} + 2C_{12}, \quad 0 < C_{44},$$
$$0 < C_{11} - C_{12}, \quad C_{12} < B < C_{11}, \tag{1}$$

and thus we conclude that these moduli are elastically stable [20].

The computed bulk modulus using elastic constants is nearly identical to the value obtained by fitting $P(V/V_0)$. This demonstrates the precision of our computations. The dependency of elastic moduli on pressure for Cs_2SnBr_6 and Rb_2SnBr_6 is shown in Fig. 5. When the pressure increased, all estimated elastic moduli rise monotonically, but the increase in C_{44} is less sensitive to pressure. The reduced hardness of these compounds is explained by their weaker elastic constants. Table III contains a list of the mechanical characteristics (bulk modulus, shear modulus, Young's modulus, Poisson's ratio, universal anisotropy, and B_H/G_H ratio) determined using GGA-PBESOL and the Voigt [21], Reuss [22], and Hill [23] approximations. When the Poisson's ratio exceeds the threshold value of 0.25, these materials tend to have metallic bonding
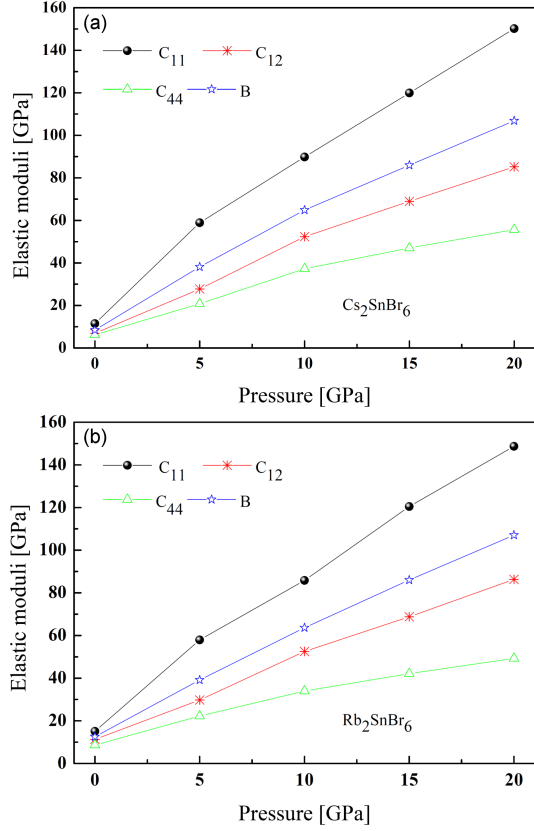
Fig. 5. The dependence of elastic moduli on pressure for (a) Cs_2SnBr_6 and (b) Rb_2SnBr_6.

Fig. 6. The dependence on direction of (a) Poisson's ratio, (b) Young's modulus, (c) linear compressibility and (d) shear modulus of Rb_2SnBr_6.

Fig. 7. Band structures of Rb_2SnBr_6 and Cs_2SnBr_6 using (a) GGA-PBESOL and (b) the HSE hybrid functional..

characteristics. Interatomic forces are important, which is explained by the fact that the Poisson coefficient value is in the range 0.25–0.5. The universal anisotropy and B_H/G_H ratio show that these materials are ductile and anisotropic, with Rb_2SnBr_6 having the strongest anisotropy.

For a cubic crystal, the Voigt and Reuss limit for the bulk and shear modulus are given [21–23] as, respectively,

$$B = \frac{B_R + B_V}{2} \tag{2}$$

and

$$G = \frac{G_R + G_V}{2}. \tag{3}$$

Young's modulus and Poisson's ratio can be obtained using the following relations

$$E = \frac{9GB}{3B + G} \tag{4}$$

and

$$\sigma = \frac{3B - 2G}{2(3B + G)}. \tag{5}$$

To see the previously mentioned parameters in 3D directions, we use the ELATE program [24]. For Rb_2SnBr_6, Fig. 6 shows how Poisson's ratio, Young's modulus, linear compressibility, and shear modulus vary in a given direction. Any deviation from the 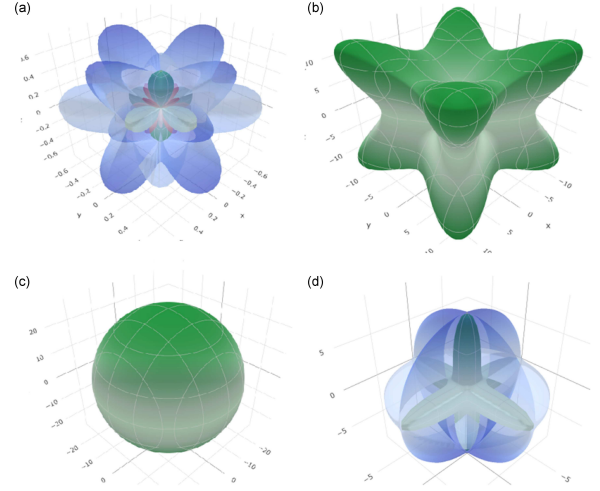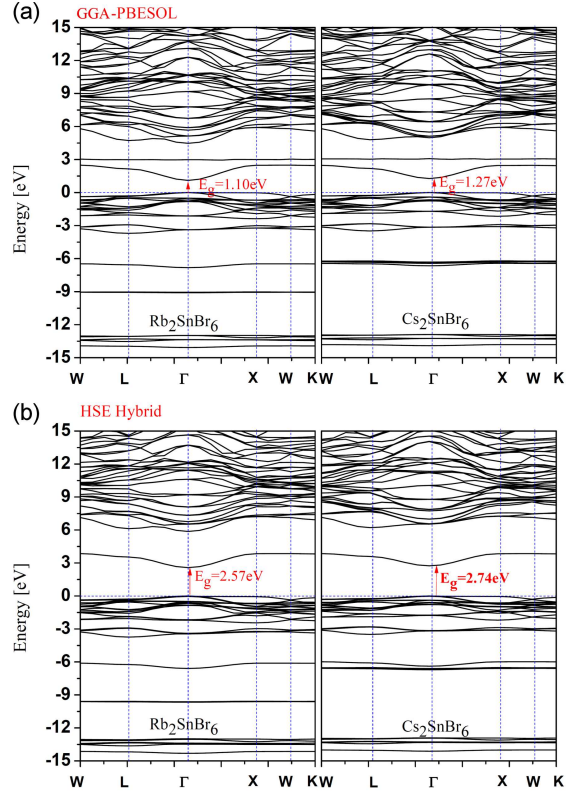spherical shape of an isotropic substance denotes anisotropy. While linear compressibility is isotropic, Young's modulus, shear modulus, and Poisson's ratio are all anisotropic. Additionally, Table IV lists the expected maximum and minimum values of Young's modulus, linear compressibility, shear modulus, and Poisson's ratio

TABLE V

The direct and indirect band gaps of Rb_2SnBr_6 and Cs_2SnBr_6

Material		$E_{\Gamma-\Gamma}$	$E_{\Gamma-X}$	$E_{\Gamma-L}$	E_{X-X}	E_{L-L}
Rb_2SnBr_6	GGA-PBESOL					
	E_0 [eV]	1.11	2.48	2.15	2.5	2.45
	$\alpha \times 10^{-2}$ [eV/GPa]	−8.90				
	$\beta \times 10^{-3}$ [eV/GPa^2]	2.30				
	HSE03 hybrid					
	E_0 [eV]	2.58	3.85	3.54	3.90	3.84
Cs_2SnBr_6	GGA-PBESOL					
	E_0 [eV]	1.27	2.46	2.19	2.48	2.49
	$\alpha \times 10^{-2}$ [eV/GPa]	−10.25				
	$\beta \times 10^{-3}$ [eV/GPa^2]	2.93				
	HSE03 hybrid					
	E_0 [eV]	2.74	3.84	3.59	3.88	3.82
	Other					
	E_0 [eV]	4.492 [19]				
		2.36 [27]				
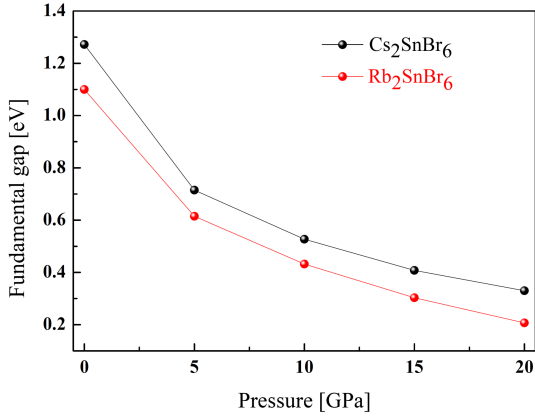
Fig. 8. The pressure effect on fundamental band gap for Rb_2SnBr_6 and Cs_2SnBr_6.

for Cs_2SnBr_6 and Rb_2SnBr_6. These numbers support the anisotropy of the other characteristics and demonstrate the isotropic linear compressibility.

3.3. Electronic band structure

We will discuss the electronic band structure and the projected density of states. Figure 7 represents the band structure of Cs_2SnBr_6 and Rb_2SnBr_6 made with GGA-PBESOL and the HSE hybrid functional. Cs_2SnBr_6 and Rb_2SnBr_6 show a direct Γ–Γ band gap for GGA-PBESOL (1.27 eV and 1.10 eV) and the HSE hybrid functional (2.74 eV and 2.57 eV) and it explains their semiconducting character. The study conducted on the band structure of Rb_2SnBr_6 by M. Razzaq, M. Tarikul [11] using the PBE potential indicates a direct band gap of 1.22 eV. Previously reported studies show that the GGA-PBESOL approach is in good agreement with the case of double perovskites [25, 26].

In Table V, we report the direct and indirect band gaps of Rb_2SnBr_6 and Cs_2SnBr_6 using GGA-PBESOL and the HSE hybrid functional. We give the theoretical value of the Γ–Γ band gap for Cs_2SnBr_6 [19, 27]. Figure 8 displays the pressure effect on the fundamental direct band gap for X_2SnBr_6 (X = Rb, Cs). The band gap decreases monotonously with increasing pressure for both compounds.

Figure 9 visualizes the partial and total densities of states for Rb_2SnBr_6 and Cs_2SnBr_6. The Br-p state mostly contributes to the upper valence band around the Fermi level. The Cs, Rb, and Sn sites are empty in the first conduction band; consequently, a transition occurs from the Br-p state to the Cs, Rb, or Sn sites. However, the Sn-s state is dominant at the conduction band minima, confirming that the Sn atom has an ionic bonding nature with the Br atom. The hybridization below the Fermi level located between −4 eV and −2.5 eV comes from Sn-p site and Br-p site, which explains the covalent bonding. Rb_2SnBr_6 and Cs_2SnBr_6 have symmetrically equivalent Sn sites in their unit cell. The flat band at 3 eV appears in GGA-PBESOL, corresponds to a band of Sn-s site, and it is confirmed by projected density of states (PDOS).

3.4. Optical characteristics

The crystalline structure of a material affects its optical characteristics. Isometric cubic crystal is optically isotropic. The reflectivity, absorption, and loss function spectra for Cs_2SnBr_6 and Rb_2SnBr_6 are shown in Fig. 10 as a function of wavelength. We distinguish a high-loss region having a wavelength located in the range of 42.4–127.24 nm. The wavelength of the low loss function is less than 42.4 nm and greater than 127.24 nm. The maximum loss reaches the value 3.33 (3.12)

TABLE VI

The main optical transitions and imaginary part peaks of Cs_2SnBr_6 and Rb_2SnBr_6.

Peaks	$W \rightarrow L$	$L \rightarrow \Gamma$	$\Gamma \rightarrow X$	$X \rightarrow W$	$W \rightarrow K$
			Cs_2SnBr_6		
$E = 2.64$ eV	$V_1 \rightarrow C_1, V_2 \rightarrow C_1,$ $V_3 \rightarrow C_1$	$V_5 \rightarrow C_1, V_6 \rightarrow C_1$	$V_6 \rightarrow C_1, V_5 \rightarrow C_1,$ $V_3 \rightarrow C_1$		
$E = 5.34$ eV	$V_1 \rightarrow C_3, V_2 \rightarrow C_3,$ $V_3 \rightarrow C_3, V_4 \rightarrow C_3,$ $V_6 \rightarrow C_3$	$V_5 \rightarrow C_3, V_6 \rightarrow C_3,$ $V_1 \rightarrow C_4, V_3 \rightarrow C_4,$ $V_1 \rightarrow C_6$	$V_1 \rightarrow C_4, V_1 \rightarrow C_6,$ $V_3 \rightarrow C_6$		
$E = 6.74$ eV	$V_3 \rightarrow C_4, V_4 \rightarrow C_4,$ $V_5 \rightarrow C_4$	$V_6 \rightarrow C_7, V_6 \rightarrow C_5,$ $V_5 \rightarrow C_7, V_5 \rightarrow C_6$	$V_6 \rightarrow C_7, V_5 \rightarrow C_7,$ $V_6 \rightarrow C_6, V_3 \rightarrow C_6,$ $V_3 \rightarrow C_5, V_1 \rightarrow C_6,$		
$E = 7.47$ eV	$V_6 \rightarrow C_7, V_6 \rightarrow C_6,$ $V_5 \rightarrow C_6, V_4 \rightarrow C_7,$ $V_3 \rightarrow C_7$		$V_6 \rightarrow C_7, V_4 \rightarrow C_7,$ $V_3 \rightarrow C_7$	$V_3 \rightarrow C_6, V_4 \rightarrow C_6,$ $V_2 \rightarrow C_7$	$V_2 \rightarrow C_7, V_5 \rightarrow C_6$
			Rb_2SnBr_6		
$E = 2.54$ eV	$V_1 \rightarrow C_1, V_2 \rightarrow C_1,$ $V_3 \rightarrow C_1$	$V_5 \rightarrow C_1, V_6 \rightarrow C_1$ $V_3 \rightarrow C_1$		$V_1 \rightarrow C_1, V_2 \rightarrow C_1$	
$E = 5.13$ eV	$V_1 \rightarrow C_3, V_2 \rightarrow C_3,$ $V_5 \rightarrow C_3, V_4 \rightarrow C_3,$ $V_6 \rightarrow C_3$	$V_5 \rightarrow C_3, V_3 \rightarrow C_6,$ $V_1 \rightarrow C_4, V_3 \rightarrow C_4$	$V_1 \rightarrow C_3, V_1 \rightarrow C_6,$ $V_1 \rightarrow C_4, V_3 \rightarrow C_4,$ $V_3 \rightarrow C_3$		
$E = 6.5$ eV	$V_1 \rightarrow C_7, V_2 \rightarrow C_7,$ $V_3 \rightarrow C_7, V_4 \rightarrow C_4$ $V_5 \rightarrow C_4$	$V_6 \rightarrow C_7, V_6 \rightarrow C_5,$ $V_5 \rightarrow C_7, V_6 \rightarrow C_4$	$V_1 \rightarrow C_6, V_4 \rightarrow C_5,$ $V_3 \rightarrow C_6, V_6 \rightarrow C_7,$ $V_5 \rightarrow C_7$	$V_6 \rightarrow C_4, V_2 \rightarrow C_5$	
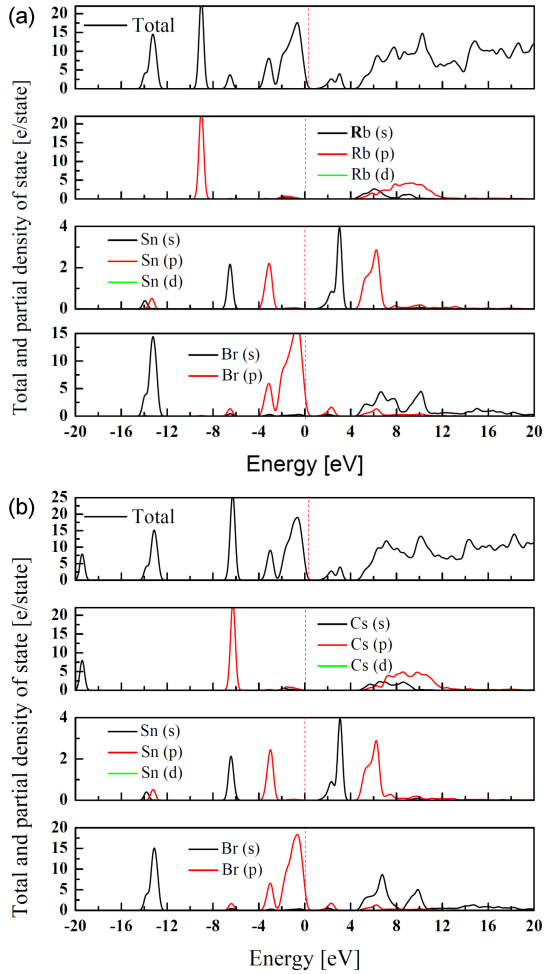
Fig. 9. Total and partial densities of states of (a) Rb_2SnBr_6 and (b) Cs_2SnBr_6.
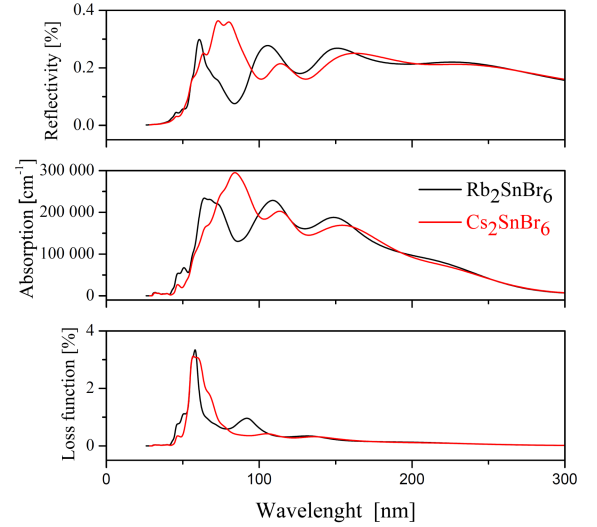
Fig. 10. (a) Reflectivity, (b) absorption and (c) loss function of Rb_2SnBr_6 and Cs_2SnBr_6.

at 58.24 nm (56.9 nm) for Rb_2SnBr_6 (Cs_2SnBr_6). The photo transition energies from the maximum valence band to the minimum conduction band under intense ultraviolet light irradiation are responsible for the absorption peaks. For Cs_2SnBr_6, the high absorption value is 295074 cm^{-1} (234133 cm^{-1}) at 84.13 nm (64.2 nm) (Rb_2SnBr_6). In fact, Cs_2SnBr_6 and Rb_2SnBr_6 have a narrow band gap and absorb the most extreme ultraviolet (EUV) radiation. As a result, they are a strong contender for photocatalysis in this EUV light domain. Beginning at a wavelength of about 34.5 nm, the reflectance
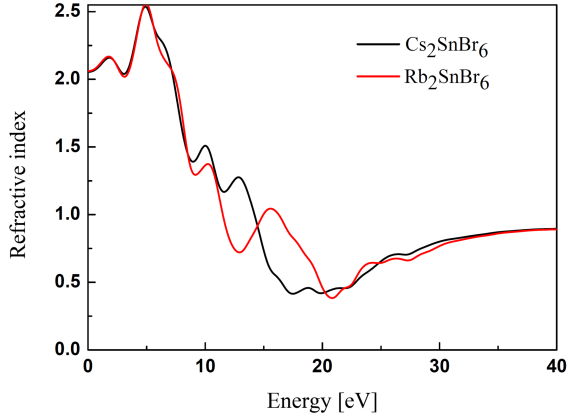
Fig. 11. Refractive index of Rb_2SnBr_6 and Cs_2SnBr_6.

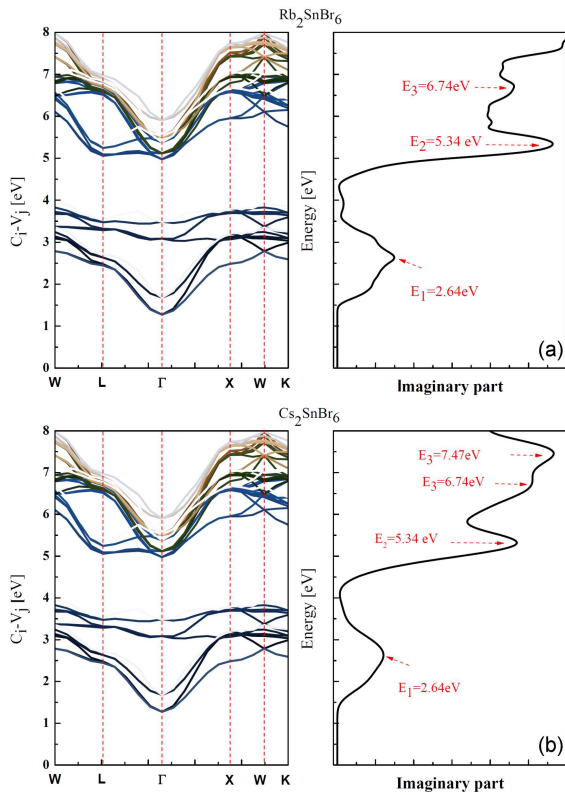Fig. 12. Imaginary part of dielectric function (right) and transition energy (left) of (a) Rb_2SnBr_6 and (b) Cs_2SnBr_6.

through the material, because it is proportional to the electron density and is greater when the bonds between the atoms are covalent.

We display the imaginary part of the dielectric function $C_j - V_i$ and the transition energy $E(k) = E_{C_j}(k) - E_{V_i}(k)$ for both Rb_2SnBr_6 and Cs_2SnBr_6 in Fig. 12. The first two excitonic states with strong oscillator strength appeared at 2.64 eV and 5.34 eV (2.54 eV and 5.13 eV) for $Cs_2SnBr_6(Rb_2SnBr_6)$. These peaks mainly originate from the optical transitions between points W and L in the Brillouin zone (BZ). In Table VI, we summarize that Rb_2SnBr_6 and Cs_2SnBr_6 are the major contributions to the optical transitions from the six top valence bands to the seven lower conduction bands. The use of Cs_2SnBr_6 and Rb_2SnBr_6 as windows and lenses is made possible by their optical properties. Cs_2SnBr_6 and Rb_2SnBr_6 are suitable candidates for photovoltaic applications due to the band gap size in the region of 1 to 2 eV utilizing GGA-PBESOL and the amount of EUV light absorption.

4. Conclusion

We studied the hexahalometallate Rb_2SnBr_6 and Cs_2SnBr_6 using the plane wave pseudopotential, within GGA-PBESOL and the HSE hybrid functional. The internal coordinate of the Br atom in Cs_2SnBr_6 is lower than that of the Br atom in Rb_2SnBr_6 because it is inversely proportional to the radius of Cs and Rb. The elastic constants of Rb_2SnBr_6 and Cs_2SnBr_6 are significantly smaller due to their lower Coulomb forces and therefore they are fairly soft. The linear compressibility of Rb_2SnBr_6 and Cs_2SnBr_6 is isotropic, while Young's modulus, shear modulus and Poisson's ratio are anisotropic, and anisotropy is more pronounced in Rb_2SnBr_6. The band gap size and the amount of absorption in EUV light suggest that Rb_2SnBr_6 and Cs_2SnBr_6 are good candidates for photovoltaic applications. The hybridization from the Sn-p and Br-p states below the Fermi level explains their covalent bonding. It turns out that the lower electronegativity of Cs compared to the electronegativity of Rb, the higher band gap of Rb_2SnBr_6 compared to that of Cs_2SnBr_6. The refractive index is more important for covalent atomic bonds.

References

[1] A.S. Verma, A. Kumar, *J. Alloys Compd.* **541**, 210 (2012).

[2] K. Rössler, J. Winter, *Chem. Phys. Lett.* **46**, 566 (1977).

of Rb_2SnBr_6 (Cs_2SnBr_6) reaches a maximum value of 0.29 (0.36) at 60.85 nm (73.09 nm). In Fig. 11, we present the effect of photon energy on the refractive index. The static refractive index is 2.06 (2.05) for $Rb_2SnBr_6(Cs_2SnBr_6)$. The experimental refractive index is 1.825 for Rb_2SnBr_6 calculated by N. Wruk et al. [9]. It reaches the maximum value 2.56 (2.53) at 4.9 eV (4.87 eV) for $Rb_2SnBr_6(Cs_2SnBr_6)$. The minimum value obtained is 0.38 (0.41) at 21.02 eV (17.52 eV) for $Rb_2SnBr_6(Cs_2SnBr_6)$. The refractive index is more important when the photons move

[3] A. Kojima, K. Teshima, Y. Shirai, T. Miyasaka, *J. Am. Chem. Soc.* **131**, 6050 (2009).

[4] L. Krache, M.A. Ghebouli, B. Ghebouli, S. Alomairy, M. Reffas, M. Fatmi, T. Chihi, *Phys. Status Solidi B* **259**, 2200042 (2022).

[5] X. Huang, T.R. Paudel, P.A. Dowben, S. Dong, E.Y. Tsymbal, *Phys. Rev. B* **94**, 195309 (2016).

[6] G.E. Eperon, G.M. Paterno, R.J. Suttonn, A. Zampetti, A.A. Haghighirad, F. Cacialli, H.J. Snaith, *J. Mater. Chem. A* **3**, 19688 (2015).

[7] M.A. Ghebouli, B. Ghebouli, L. Krache, S. Alomairy, M. Fatmi, T. Chihi, M. Reffas, *Bull. Mater. Sci.* **45**, 1 (2022).

[8] M.G. Ju, M. Chen, Y. Zhou, H.F. Garces, J. Dai, L. Ma, N.P. Padture, X.C. Zeng, *ACS Energy Lett.* **3**, 297 (2018).

[9] N. Wruk, J. Pelzl, G.A. Saundersn, T. Hailing, *J. Phys. Chem. Solids* **46**, 1235 (1985).

[10] Y. Tang, J. Zhang, X. Zhong, Q. Wang, H. Zhang, C. Ren, J. Wang, *Solar Energy* **190**, 272 (2019).

[11] M. Razzaq, M. Tarikul, *Global J. Mater. Sci. Eng.* **2**, 1 (2020).

[12] M.D. Segall, P.J.D. Lindan, M.J. Probert, C.J. Pickard, P.J. Hasnip, S.J. Clark, M.C. Payne, *J. Phys. Condens. Matter* **14**, 2717 (2002).

[13] D. Vanderbilt, *Phys. Rev. B* **41**, 7892 (1990).

[14] J.P. Perdew, K. Burke, M. Ernzerhof, *Phys. Rev. Lett.* **77**, 3865 (1996).

[15] H.J. Monkhorst, J.D. Pack, *Phys. Rev. B* **13**, 5188 (1976).

[16] T.H. Fischer, J. Almlof, *J. Phys. Chem.* **96**, 9768 (1992).

[17] A. Kaltzoglou, M. Antoniadou, A.G. Kontos, C.C. Stoumpos, D. Perganti, E. Siranidi, V. Raptis, K. Trohidou, V. Psycharis, M.G. Kanatzidis, P. Falaras, *J. Phys. Chem. C* **120**, 11777 (2016).

[18] G. Yuan, S. Huang, J. Niu, S. Qin, X. Wu, H. Ding, A. Lu, *Solid State Commun.* **275**, 68 (2018).

[19] Y. Chang, T. Yoon, T. Lim, P. Koh, M. Tuh, *J. Alloys Compd.* **779**, 497 (2019).

[20] G.V. Sin'ko, N.A. Smirnov, *J. Phys. Condens. Matter* **14**, 6989 (2002).

[21] W. Voigt, *Lehrbuch der Kristallphysik*, Teubner, Leipzig 1928.

[22] A. Reuss, Z. Angew, *Math. Mech.* **9**, 49 (1929).

[23] R. Hill, *Proc. Phys. Soc. London A* **65**, 349 (1952).

[24] R. Gaillac, P. Pullumbi, F. Coudert, *J. Phys. Condens. Matter.* **28**, 275201 (2016).

[25] M. Pazoki, T.J. Jacobsson, A. Hagfeldt, G. Boschloo, T. Edvinsson, *Phys. Rev. B* **93**, 144105 (2016).

[26] M.R. Filip, F. Giustino, *Phys. Rev. B* **90**, 245145 (2014).

[27] H. Huang, Z. Jiang, S. Luo, *Chinese Phys. B* **26**, 096301 (2017).